Three Dimensional Design of Silver Nanoparticle Assemblies Embedded in Dielectrics for Raman Spectroscopy Enhancement and Dark-Field Imaging

Robert Carles,* Cosmin Farcau, Caroline Bonafos, Gérard Benassayag, Maxime Bayle, Patrizio Benzo, Jesse Groenen, and Antoine Zwick

Groupe Nanomat—CEMES-CNRS—Université de Toulouse, 29 rue Jeanne Marvig, BP 94347, 31055 Toulouse Cedex 4, France

ABSTRACT A strategy to design and fabricate hybrid metallic-dielectric substrates for optical spectroscopy and imaging is proposed. Different architectures consisting of three-dimensional patterns of metallic nanoparticles embedded in dielectric layers are conceived to simultaneously exploit the optical interference phenomenon in stratified media and localized surface plasmon resonances on metal nanoparticles. These structures are based on a simultaneous control of opto-electronic properties at three scales (3S) (~2/20/200 nm) and along three directions (3D). By ultralow energy ion implantation through a microfabricated stencil we precisely control the size, density, and location of silver nanoparticles embedded in silica/silicon thin films. Elastic (Rayleigh) and inelastic (Raman) scattering imaging assisted by simulations were used to analyze the optical response of these "3S—3D" patterned layers. The reflectance contrast is strongly enhanced when resonance conditions between the stationary electromagnetic field in the dielectric matrix and the localized plasmon resonance in the silver nanoparticles are realized. The potential of these 3S—3D metal—dielectric structures as surface-enhanced Raman scattering substrates is demonstrated. These novel kinds of plasmonic-photonic architectures are reproducible and stable; they preserve flat and chemically uniform surfaces, offering opportunities for the development of efficient and reusable substrates for optical spectroscopy and imaging enhancement.

KEYWORDS: silver nanoparticles · plasmon resonance · optical spectroscopy · SERS · optical reflectance contrast · ion implantation · dark-field imaging

Developing highly sensitive optical sensors based on localized surface plasmon resonance (LSPR) or surface-enhanced Raman scattering (SERS) still attracts much attention[1,2] due to these types of sensors' noninvasive character and their high sensitivity. Since its discovery[3] on pyridine molecules adsorbed on rough silver surfaces, SERS has particularly received a great deal of attention as a powerful analytical technique for molecular spectroscopy, biomolecule recognition, and ultrasensitive detection, down to a single molecule.[4,5] To exploit the giant enhancement of electromagnetic coupling at the vicinity of metallic nanoparticles (NPs), one has to maximize the coupling matrix element between light and electronic excitations. According to the so-called "golden rule" for the transition probability between two quantum states, one also has to enhance in the appropriate spectral range and at the appropriate position the density of intermediate or final states. The coupling reaches its maximum value in resonant conditions, thus defining the appropriate energy range of the incident and scattered photons, and the spatial density of states of these photons is considerably increased by their interaction with localized surface plasmons.

In practice, the patterning[6−10] of the supporting devices has to be controlled at different scales ("3S"): (i) the device patterning must thus be controlled at the nanometer scale because both mechanisms generally invoked[11] for SERS, the so-called "electromagnetic" and "chemical" ones, are efficient when the distance between the metal surface and the scatter center is in the tunneling or "near-field" range;[12] (ii) the damping of the plasmon resonance is reduced when the size of the NPs exceeds a few tens of nanometers; and (iii) the enhancement can be considerably increased by exploiting bilayer interference-enhanced Raman spectroscopy (BIERS):[13] in this "far-field" regime, layer thicknesses are of few hundreds of nanometers. In this context it is particularly interesting to develop novel approaches for simultaneously controlling the geometry at the submicrometer scale and at the nanoscale. These approaches will offer new opportunities for the design of optoelectronic devices operating not only in the far field (guiding, interference, and grating effects) but also in the near-field regime (electron and photon tunneling, localized vibrational modes,

* Address correspondence to robert.carles@cemes.fr.

Received for review July 21, 2011 and accepted October 11, 2011.

Published online October 11, 2011
10.1021/nn202767p

localized plasmons, localized density of photon states in "hot spots").[12]

The limitation for fabricating such plasmonic substrates is due to the drastic requirement of controlling, on large areas in a reproducible way, a well-defined spacing between metallic nanostructures and molecules. Then controlling their shape, ordering and spacing at different scales is a real challenge, particularly at the nanoscale.

Important requirements also concern the sensitivity, uniformity, and reproducibility of the response, high stability, and low cost for commercial applications. The use of silver nanoparticles (Ag-NPs) instead of gold NPs offers the advantage of a better plasmonic enhancement because of lower interference between intraband and interband electronic transitions.[14] Many effective ways have been explored[9,15,16] for the synthesis of Ag plasmon-active surfaces as an aggregation of colloids, electrochemically roughened electrodes, atom beam sputtering, or pulsed laser deposition. Most of the currently available lithographic techniques are developed for the fabrication of two-dimensional (2D) metallic nanostructure arrays and often carry with them limitations that prohibit their widespread use for biological spectroscopy and imaging.[15−17] Recently we have shown that low energy ion implantation can be a promising technique for the wafer-scale fabrication of Ag NPs planar arrays embedded in a silica (SiO_2) on a silicon substrate.[18,19] We have shown that a postannealing process strongly limits the silver oxidation process which otherwise excludes the use of Ag NPs on free surfaces.[20] Second, controlling the kinetic energy of the implanted ions in the keV range offers the possibility to control in the nanometer range the subsurface positioning of the metal nanostructures (Z-patterning).

In this work, we propose a novel class of plasmonic substrates containing subsurface gratings (1D and 2D) made of Ag NP assemblies. These are obtained by combining low energy ion implantation with a soft lithography stencil technique. We show by theoretical analyses and experiment how such three scale−three dimension ("3S−3D") patterns of metal-dielectric composites can be exploited as substrates for enhancing the efficiency for light scattering, diffraction, or imaging.

RESULTS AND DISCUSSION

Growth and Structural Properties. Typical transmission electron microscopy (TEM) cross-section and plane-view images of the Ag NPs embedded in the dielectric film are shown in Figure.1. Figure 1a is a 3D montage combining the cross-section view (*z* axis) and the plane-view (*x*, *y*) for the lowest implantation dose. One observes a delta-layer of single crystalline (as revealed by high resolution TEM) spherical Ag NPs.[19] Their mean diameter and spacing, and the distance between the layer and the free surface of silica, are all in the nanometer range (Figure 1). This distance is controlled by the kinetic energy of the implanted ions, thus offering an original way to define an optical spacer between metallic particles and the free surface of the sample over a large area. The size and density of the particles can be tuned by modifying all the implantation parameters: kinetic energy, dose, and current. In Figure1 panels b and c, one sees that the size of the particles can be increased by 1 order of magnitude (from a few nanometers to 15 nm), while preserving a localization of the built-in plasmonic antenna at the very near vicinity of the surface. The inset in Figure 1b shows that at low energy implantation, the particles are crystalline and spherical; this shape is expected from a diffusion process in a homogeneous matrix. In this paper we shall be concerned only with samples obtained with different Ag^+ doses, but with a constant very low energy of implantation (3 keV), and using the same current (5 μA); the low value of the acceleration voltage ensures negligible matrix and sputtering effects during the implantation process. In Figure 1b, one observes in the cross-section image the preservation of a dielectric spacer (few nanometers) between the metallic particle and the free surface of the layer; in the plane view, one notes that the mean separation distance is much larger than their diameter *D*, with a factor around 10; this will support in our calculations the approximation of a negligible interparticle coupling for both vibrational and electronic properties.

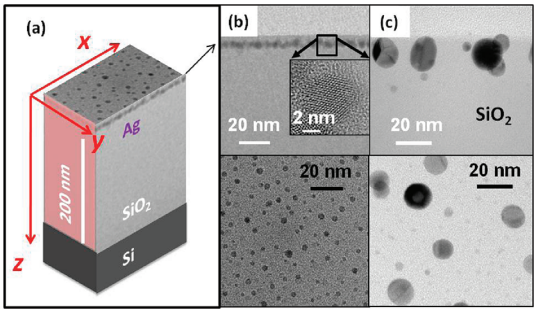

Figure 1. (a) 3D montage coupling the cross-section view (*z* axis) and the plan-view (*x*, *y*) of our composite system; (b) cross-sectional TEM image (defocused bright field) of the sample implanted at 3 keV with 4.7 × 10^{15} ions/cm^2 and (c) at 20 keV with 3.1 × 10^{16} ions/cm^2. In inset of panel b, HREM image of an isolated Ag nanocrystal; (d and e) associated plan-view observations.

The destructive interference of the waves reflected at the different interfaces of the dielectric slab gives rise to Fabry−Pérot oscillations in the reflection. By choosing an appropriate dielectric thickness, the reflectance is at minimum at specific wavelengths and simultaneously the electric field is at maximum at the free surface. This will favor the coupling of incident photons of well-defined energy with both the Ag NPs which are buried at the vicinity of this surface and any nano-object (molecule, quantum dot, *etc.*) deposited

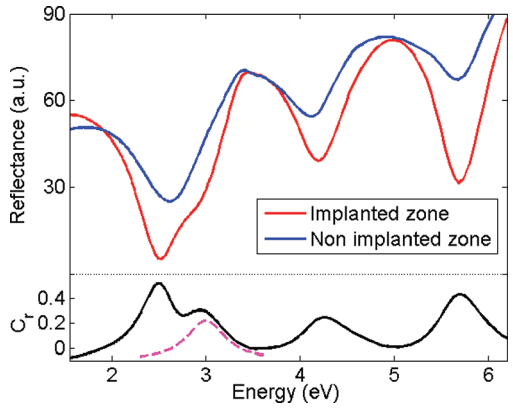

Figure 2. Reflectance spectra of a SiO/Si sample implanted at 3 keV with 9.4 × 10^{15} ions/cm^2. The reflectance contrast (black line) is deduced from the spectra of an implanted zone (red line) and that of a nonimplanted one (blue line), as described in the text (eq 2). The dotted line is a Lorentzian fit of the data to extract the plasmon resonance contribution.

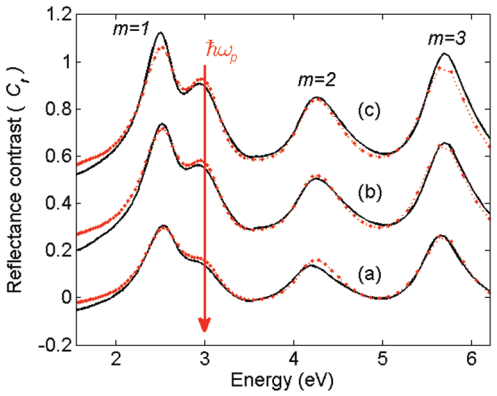

Figure 3. Reflectivity contrast spectra of three samples implanted at 3 keV with different doses 4.7, 7.05, and 9.4 × 10^{15} ions/cm^2 (from bottom to top): experiment results in continuous black lines; theoretical results in red dots. The curves have been vertically translated for clarity.

on it. Because of the high value of the refractive index of the Si substrate, the appropriate energy of reflectivity minima are essentially defined by the thickness t and effective refractive index n of the deposited dielectric layer, and by the refraction angle θ_r. These minima are assigned to the different orders m of the bilayer destructive interference phenomenon and the respective photon energies E_m are given by

$$E_m = \left(m + \frac{1}{2}\right)\frac{hc}{2nt\cos\theta_r} \quad (1)$$

where h is the Planck constant and c the light velocity in vacuum.

A typical UV−visible reflectivity spectrum recorded in backscattering geometry ($\theta_r \approx 0$) on a SiO_2/Si heterostructure, is shown in Figure 2 (blue line). On bare SiO_2 ($n \approx 1.46$), from the first-order ($m = 1$) reflectivity minimum observed at $E_1 = 2.63$ eV, one gets $t \approx 245$ nm, in agreement with the value measured by TEM ($t \approx 240$ nm; see Figure 1a). As a matter of fact, one gets the same value of t from the other observed reflectivity minima, $E_2 = 4.1$ eV and $E_3 = 5.7$ eV.

The presence of buried Ag NPs is indicated in the reflectivity response (red line in Figure 2) by a deepening of the reflectance minima. One clearly observes that a single plane of Ag NPs greatly affects the antireflective effect because of its location at a depth where the electric field is at maximum. This strong perturbation is more evidenced by evaluating the contrast C_r of the reflectivity signal, defined as follows:

$$C_r = \frac{R_0 - R}{R_0} = \frac{A_{Ag} + \Delta A_{Si}}{R_0} \quad \text{with}$$
$$\Delta A_{Si} = (A - A_0)_{Si} \quad (2)$$

where $R_0(A_0)$ is the reflectivity (absorption, respectively) corresponding to a nonimplanted sample and $R(A)$ its value for an implanted sample. Equation 2 shows that the C_r spectrum will reflect the absorption by both the Ag NPs (A_{Ag}) and the Si substrate (ΔA_{Si}) because the plane of Ag NPs induces optical changes in the bilayer. Moreover, according to eq 2 one notes that the signature of NPs in the reflectance contrast will be greatly enhanced at the vicinity of the antireflection condition because R_0 is at minimum. This offers an efficient way to check the modifications of the real and imaginary parts of the effective index n of the dielectric layer, as illustrated in Figure 3 where the C_r experimental spectra corresponding to three Ag^+ doses are reported . In all the spectra, the localized surface plasmon resonance (LSPR) of the monolayer of dispersed Ag NPs develops as a well-defined peak around 3.0 eV with a Lorentzian shape. This energy coincides with the expected value for absorption by an isolated Ag spherical particle embedded in SiO_2,[14] and retardation or collective effects are expected to be negligible for nanometer sized and highly dispersed particles. In normal incidence ($\theta_r \approx 0$), the plasmon peak is clearly shifted from the $m = 1$ interference maximum, and one can thus estimate its full-width at half-maximum (fwhm) for the three samples: $\Gamma \approx 0.5$ eV.

When the diameter D of a metallic nanoparticle is much lower than the electronic mean free path (52 nm in Ag at room temperature) and greater than the Fermi wavelength ($\lambda_F \approx 0.5$ nm in Ag) which defines the classical-quantum transition, that is, typically $50 \gg D \gg 1$ nm, the intrinsic dominant channel for a plasmon decay in electron−hole pairs (Landau damping) is the electron surface scattering process (τ_S). Taking into account that radiation damping is negligible in such particles which sizes much lower than the wavelength, the plasmon lifetime is written as follows:[14]

$$\tau^{-1} = \tau_0^{-1} + \tau_S^{-1} \quad \text{with} \quad \tau_S^{-1} = 2g_S\frac{v_F}{D} \quad (3)$$

in which $\tau_0 = \hbar/\Gamma_0$ is the bulk contribution and g_S a numerical factor. Using the Fermi velocity in silver,

TABLE 1. Comparison between Optical Spectroscopy (Reflectance Contrast and Raman) and TEM Observations for Different Si/SiO_2 Samples Implanted with Ag^+ Ions

	thickness t (nm)		dose f (10^{15} cm^{-2})			diameter $\bar{D}$ (nm)		
sample	TEM	reflectance	implanted	TEM	reflectance	TEM	reflectance	Raman
D1	238(12)	242(1)	4.70	1.8 (0.5)	2.8	4.6 (0.5)	3.0 (0.2)	3.8 (0.2)
D2	238(12)	242(1)	7.05		4.0	5.8 (0.5)	4.0 (0.2)	3.9 (0.2)
D3	234(12)	242(1)	9.40		4.5	5.4 (0.5)	4.4 (0.2)	4.5 (0.2)

$v_F = 1.39 \times 10^6$ m·s^{-1}, one finally obtains the following relation between the diameter D of a particle and the fwhm of the plasmon resonance curve:

$$D(\text{nm}) \approx g_S \frac{3.6}{(\Gamma - \Gamma_0)(\text{eV})} \quad (4)$$

The linear dependence of the width of the plasmon resonance *versus* the inverse of the mean size has been well verified experimentally for various metallic nanoparticles.[14] However very different values of the key parameters, Γ_0 and g_S, have been reported both experimentally and theoretically,[21] thus limiting the possibility of extracting absolute values of sizes from optical data. On one hand, the value of Γ_0 is greatly affected by the crystalline quality and surface roughness[22] of the bulk samples, and accurate data on noble metals are still missing.[23] On the other hand, theoretical determinations of g_S are model dependent, and reported values spread from 0.5 to 3.[14] For silver particles embedded in SiO_2, the most accurate determination of Γ_0 and g_S has been recently obtained by spectroscopic measurements on a single particle, leading to $g_S = 0.7 \pm 0.1$ and $\Gamma_0 = 0.125 \pm 0.010$ eV.[21] Using $\Gamma = 0.50 \pm 0.05$ eV in eq 3 one gets $D = 7.0 \pm 1.9$ nm for an average diameter of the Ag NPs in the three samples of Figure 3; this is in fairly good agreement with the mean size determined by TEM (see Table 1).

Simulation of the Optical Response and Size Determination. To get more accurate information at the nanoscale on the metallic particles, we have performed simulations of the reflectance contrast C_r. These will allow an understanding of the interplay between the photonic and plasmonic interactions in the 3S−3D structures and will define the most efficient architecture for enhancing the optical coupling at the plasmon frequency. Let us resume our approach that has been already reported in details elsewhere.[24] A composite layer of Ag NPs embedded in SiO_2 with a thickness equaling the mean diameter $\bar{D}$ of the NPs is considered at the vicinity of the free surface. Its effective dielectric constant is calculated within the quasi-static approximation of the classical Maxwell−Garnet theory, in which the electronic confinement effect is accounted for by introducing the surface plasmon damping according to eq 3. In the model the volume fraction of silver is expressed as a function of the incorporated silver amount f of atoms per surface unit. The propagation of electromagnetic waves in the multilayer system is described using a matrix formulation. The input data are the complex dielectric constants of substrate (Si), dielectric layer (amorphous SiO_2), and embedded metal (Ag). As recently underlined by Drachev *et al.*,[23] the optical response of an Ag-based plasmonic architecture is greatly dependent on the input data for Ag,[25,26] and one has to take care of spurious artifacts by an appropriate choice of the input data.

At a first step, the total thickness t of the dielectric layer is extracted from the bilayer interference effect in the UV range (3−6 eV): that gives for all the samples $t = 242 \pm 1$ nm. Second, the mean diameter $\bar{D}$ and the incorporated silver amount f are extracted by adjusting the shape of the theoretical curve with the experimental one. The sensitivity of the adjustment is very high because of the strong mixing between the Ag-LSPR mode and the quasi-stationnary optical mode in SiO_2: they lie in the same energy range and are both spatially confined at the vicinity of the surface. This is illustrated in Figure 4. Keeping $\bar{D}$ as a constant, the reflectance contrast increases over the whole range when increasing the incorporated silver amount f; otherwise by keeping f as a constant, the plasmon resonance progressively separates from the interference reflectivity minimum, when increasing the mean size; at the same time the interference pattern remains unchanged in the UV range.

The comparison between theory (red dots) and experiment (black curves) presented in Figure 3 shows a remarkably good agreement, both on energy position of the different features and on their intensities. In our specific samples this offers thus the possibility of an accurate determination of the mean size of the particles, position of the delta layer, and dielectric layer thickness.

The results extracted from the adjustments of the reflectance contrast are compared in Table 1 with those deduced from other experiments (TEM and Raman). Because the amount of embedded silver and the absorption cross-section of a nanoparticle are proportional to its volume, the mean diameter $\bar{D}$ has been defined from the histograms of the NPs volumes measured by TEM, namely:

$$\bar{D} = \left(\frac{1}{N} \sum_i N_i D_i^3 \right)^{1/3} \quad (5)$$

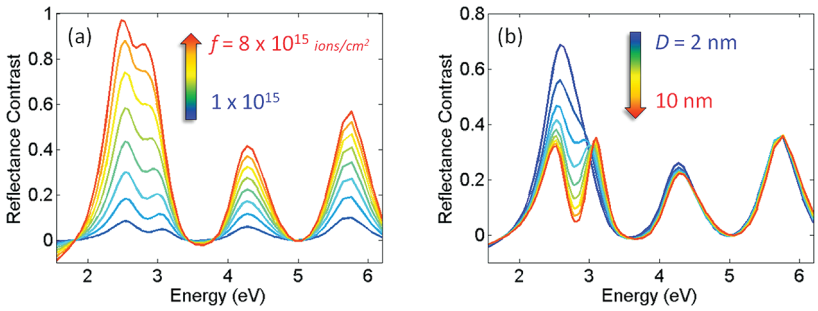

Figure 4. Evolution of the reflectance contrast of a Si/SiO_2 bilayer structure in which a plane of Ag NPs is buried at the vicinity of the free surface: (a) effect of the implanted fluence, (b) effect of the AgNPs mean diameter.

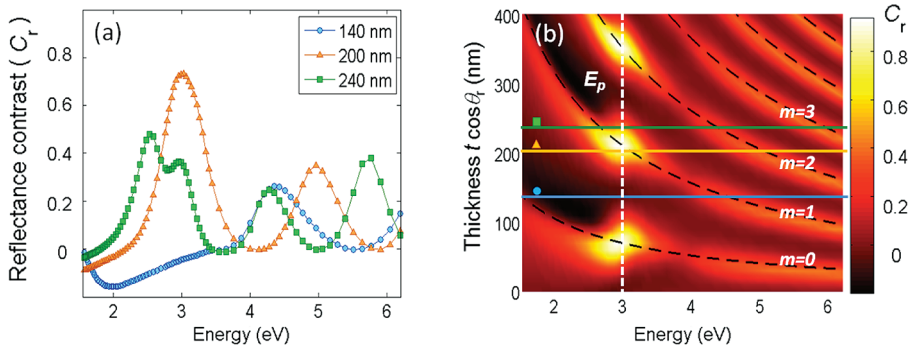

Figure 5. Simulation of the reflectance contrast C_r of a Si/SiO_2 bilayer structure in which a plane of Ag NPs ($D = 5$ nm and $f = 5 \times 10^{15}$ ions/cm^2) is buried at the vicinity of the free surface; (a) reflectance contrast spectra calculated for three typical values of the thickness corresponding to a reflectivity minimum (200 nm) or maximum (140 nm), and at the experimental record of Figure 3 and 4 (240 nm); (b) Contrast reflectance map on the plane defined by the photon energy and the total layer thickness. The vertical white dotted line corresponds to the plasmon energy, the black dotted lines correspond to the different orders m for a destructive interference.

One sees in Table 1 that the mean diameter of the particles deduced from the optical data is in good agreement with that deduced from TEM plane view observations. Finally the amount of silver incorporated in the NPs has also been determined from adjusting the theoretical spectra to the experimental ones. The values are around 40% lower than the implanted dose. This result is also in good agreement with the TEM observations. This can be due to either an indetermination in the nominal implanted dose or to an incomplete aggregation on all the Ag atoms in pure Ag NPs.[20]

The theoretical evolution of the spectrum of reflectance contrast *versus* the effective optical thickness $t \cos \theta_r$ is reported in Figure 5. It clearly shows evidence of the contrast enhancement when plasmons and photons having the same energy are simultaneously confined in the same zone. As a matter of fact, in Figure 5 the maxima are localized at crossing points between lines expressing the condition for stationary electromagnetic field in the SiO_2 dielectric matrix (see eq 1) and the line at 3.1 eV corresponding to LSPR in the metallic particles. The plasmon−photon coupling is strongly enhanced because the particles that support the plasmon oscillations are localized at maxima of the standing wave pattern. Figure 5a presents three selected horizontal cross sections through the map in Figure 5b. A remarkable effect is observed by analyzing these spectra: when an effective optical thickness of 140 nm is chosen for the SiO_2 layer containing Ag NPs, no clear signature is observed in the spectrum around 3.1 eV. Although the same amount and localization of the Ag NPs is considered, the signature of the Ag NPs LSPR becomes visible only when resonant with the bilayer interference effect. In particular this is verified in the present experimental observations (see Figure 3) where a single plane of Ag NPs located near the surface of the antireflective bilayer leads to a large modification of the reflectance contrast at the plasmon wavelength. This result demonstrates the importance of the precise 3D patterning and the potential of these metal−dielectric architectures for imaging very thin films deposited at the surface, for example, graphene monolayers.

Resonant Raman Measurements. The enhancement of the LSPR by localizing the AgNPs in the zone where the electromagnetic field is at maximum can be used for all processes mediated by plasmonic excitations. This is the case for surface enhanced Raman scattering (SERS) by the collective atomic vibrations of the particles themselves. Following eq 1 one sees that using an oblique incidence (near 50°), the first-order (m = 1) reflectivity minimum is expected at E_1 = 3.0 eV in the

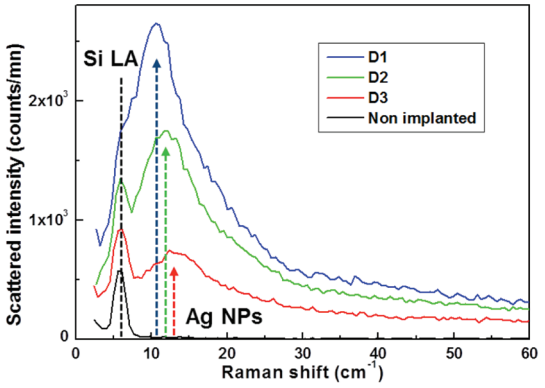

Figure 6. Raman and Brillouin spectra for samples implanted at 3 keV with different doses (see Table 1).

240 nm thick SiO_2 layer, in coincidence with the plasmon resonance. Therefore conditions for targeting a maximum, a "hot spot" in Figure 5, have been realized using in this specific geometry the 413 nm line (3.0 eV) of a Krypton laser as excitation.

Moreover, for a low frequency shift resonant conditions can be simultaneously achieved for both incident and scattered photons, leading to doubly resonant Raman spectroscopic signals for the quasi-acoustical modes. Typical spectra are reported in Figure 6. Only the Stokes side of the low-frequency range will be discussed in this paper. Two main observations are in order: (i) the signal has been recorded at very low wavenumbers (down to 4 cm^{-1}) and the Brillouin signal originating in Si substrate is clearly visible (at 6.8 cm^{-1}), (ii) the large intensity coming from a single plane of Ag NPs demonstrates the concomitant effect of plasmon resonance and optical interference. It is only in these resonant conditions that such a low density of nanometer-sized Ag NPs can be identified and analyzed by a Raman measurement. The signature of the Ag NPs consists in an asymmetric band. Its low frequency part is due to collective coherent oscillations of the Ag atoms,[27] whereas the tail *versus* high energy is attributed to single particle electronic excitations.[28] The frequencies of the different eigen modes of an isolated sphere increase with the inverse of its diameter, as follows:[27]

$$\omega_{l,n} = \eta_{l,n}\frac{v_L}{D} \quad (6)$$

where l and n are the angular and radial quantum numbers, respectively, and v_L is the longitudinal sound velocity in Ag. The numerical factor $\eta_{l,n}$ depends on the symmetry and confinement of the mode. It is now well established that the scattering is dominated by the contribution of the fundamental quadrupolar mode ($n = 0$, $l = 2$) leading to the following simple scaling relation between the diameter D of the NP and the Raman shift σ of the most intense mode:[27]

$$D\ (\text{nm}) \approx \frac{47}{\sigma\ (\text{cm}^{-1})} \quad (7)$$

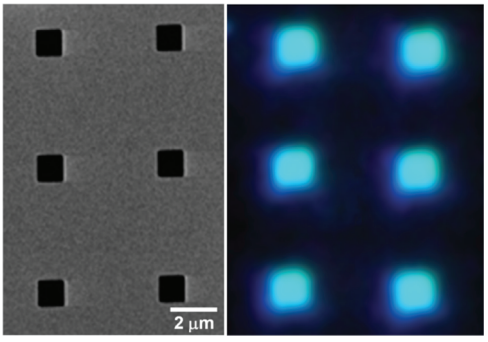

Figure 7. Optical imaging of embedded arrays of Ag NPs: (a) SEM image of the stencil used; (b) dark-field image of elastic scattering in the visible range (true colors) due to the presence of Ag-NPs sample obtained by implantation at 20 keV of 3.1 × 10^{16} Ag^+ ions/cm^2.

From the data reported in Figure 6 one can deduce a "Raman mean diameter" associated with the different samples. The results reported in Table 1 show good agreement with the TEM results. Once more one must take into account that we are concerned with a distribution of sizes. Consequently an inhomogeneous broadening affects the optical response; moreover because this response is recorded in resonant condition, the size distribution effect will concern both electronic and vibronic excitations, and their coupling.[29] It would be thus very hazardous to get accurate information solely from line shape analysis. Nevertheless, one notes in Figure 6 that the intensity increases with the implanted dose. This will be very valuable information for a quantitative Raman imaging of the buried silver amount.

Raman Imaging and Optical Resolution. By implantation through a stencil, different buried plasmonic architectures (1D and 2D gratings) made of Ag NP assemblies have been fabricated. By a careful design, all three effects described above (optical interference, plasmon resonance, and near-field coupling) can be then concurrently combined in order to maximize the efficiency of optical field enhancement at the SiO_2 surface. All the size parameters have to be adapted to a specific application. We have already underlined the benefit that can be obtained from a 3D patterning at sub-micrometer and nanometer scales. For that purpose, we showed that we can get quantitative information at both scales by analyzing simultaneously elastic (Rayleigh) and inelastic (Raman) scattering, respectively.

An example is reported in Figure 7, for a 2D array of 1 μm wide squares, with a lattice parameter of 5 μm. In Figure 7b, one observes that the dark-field image of the embedded Ag NP assemblies perfectly mirrors the stencil image contour reported in panel a; the elastic scattering dominates in the blue range testifying that it is mainly due to resonant scattering at the plasmon frequency of the Ag NPs.

The Raman spectrum of a nonimplanted area on this 2D buried grating is essentially due to the silicon substrate (Figure 8d). On the contrary, on the implanted

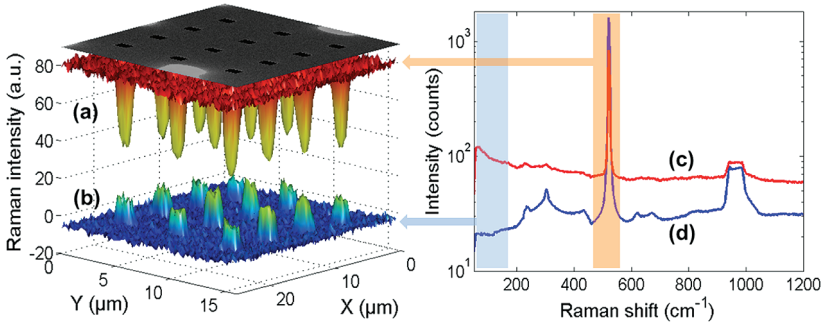

Figure 8. (Left) Raman images of embedded arrays of Ag built with the signals (same sample as in Figure 9) coming from (a) the optical phonon scattering of the Si substrate and (b) the vibrational and electronic scattering by the Ag-NPs (the vertical scale refers to intensities integrated over the spectral ranges indicated on the right). (Right) Typical Raman spectra recorded on an implanted (c) and nonimplanted zone (d) are shown (for clarity the spectra have been smoothed by averaging over several pixels of the image and the Raman intensity is presented with a log scale).

square zones, one notes that the silicon signal is reduced and superimposed on a rather continuous background revealing thus the presence of Ag NPs. The Raman signal coming from the substrate is indeed resonantly absorbed by the NPs, whereas resonant inelastic scattering by single particle excitations in these NPs occurs. Therefore we introduce here two original ways to map the presence of the embedded Ag NP architectures. First, by plotting the intensity of the optical phonon scattering of the Si substrate (480−560 cm^{-1}) one obtains the map of the buried Ag NPs due to the Ag NP resonant absorption (Figure 8a). Second by plotting the intensity of the vibrational and electronic scattering by the Ag-NPs (50−160 cm^{-1}) the same 2D maps are obtained. It is particularly relevant to use such noninvasive optical techniques to directly control the geometrical parameters at each step of the plasmonic device fabrication.

An example of a buried 1D grating of Ag NPs obtained through a stencil made of 100 nm-wide slits periodically spaced by P = 600 nm is illustrated in Figure 9a. The corresponding Raman scan of the AgNP-based grating is reported in Figure 9b. The intensity profile was fitted in Figure 9c by the convolution product of the square-wave transmission function of the stencil with a Gaussian function that accounts for the intensity profile of the focused laser beam. The chosen value of the Gaussian fwhm was 280 nm which is the resolution limit of the microscope (×100; NA = 0.9; λ = 413 nm). The very good agreement between the calculation and the experiment is a clear indication that the diffusion of Ag^{+} ions is negligible, validating the stencil technique for designing such 3S−3D multiply resonant buried plasmonic architectures.

This could open new possibilities for developing plasmonic sensors based on periodic arrays of nanostructures, with a selectivity and sensitivity improved by diffractive effects. Elastic scattering is expected to be concentrated in specific Bragg directions, and its spectral dependence should follow the resonant plasmon profile (Figures 3 and 5).

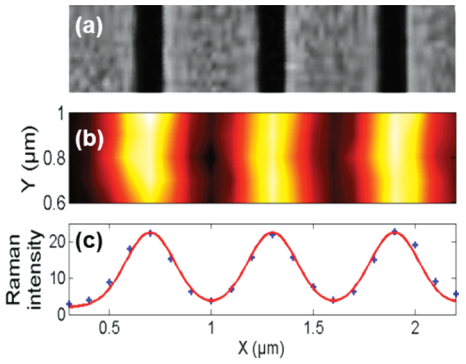

Figure 9. (a) SEM image of stencil used for fabricating an embedded grating of Ag NPs; (b) corresponding high resolution Raman image; and (c) fit of the Raman intensity profile (black dots) with the transmission function of the stencil convoluted by a Gaussian (continuous red line).

SERS Effect. Finally, Figure 10 displays results on the Raman signal originating in a micrometer-sized droplet of pure pyridine that have been deposited on the free surface of one of our plasmonic devices. The Raman signal originating from implanted areas is compared to that recorded on Ag NPs-free zones. The pyridine spectrum reported on the nonimplanted zone is similar to that of pyridine in solution: three modes at 992, 1005, and 1035 cm^{-1} are observed.[30] This spectrum is modified when the laser spot is positioned on a zone with Ag NPs: the modes located at 992 and 1035 cm^{-1} are enhanced. This evolution is difficult to analyze, since it has been shown that the surface enhancement is greatly affected by the character of the surface and the arrangements of the molecules.[9,30] If one takes into account that most of the signal comes from the volume of the liquid located around the focal point of the microscope objective (around 1 μm-thick), one can deduce that the enhancement of the signal coming from molecules located at the near vicinity of the substrate (in a sub-nanometer range), is of several orders of magnitude (around 10^3−10^4). This is typical of a SERS gain expected from the solely electromagnetic field mechanism. Indeed, in our case the chemical mechanism

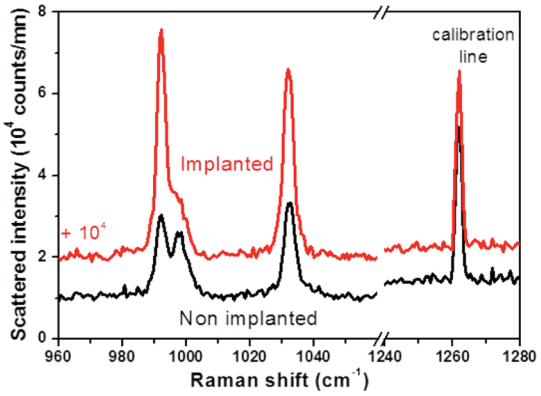

Figure 10. SERS effect on pyridine molecule deposited on an implanted sample at 3 keV with 4.7 × 10^{15} ions/cm^2.

is excluded due to the presence of a dielectric spacer between the metal surface and the molecules (see Figure 1b). In any case, it would be hazardous to calculate any enhancement factor owing to the uncertainty on the number of molecules involved in this SERS process. Although these preliminary results are promising further efforts have to be done for a precise quantitative analysis.

CONCLUSIONS

We have shown that a 3D patterning of composite materials made of metallic nanoparticles buried in a dielectric layer can be obtained in a single-step process using ion implantation through a stencil. Using low kinetic energy, ordered plasmonic architectures can be localized at the vicinity of, but below the surface, thus providing near field coupling with objects deposited on the surface.

Simulations have been performed to highlight the interplay between the photonic and plasmonic interactions in the 3S−3D structures and to identify the routes for maximizing the optical coupling for both near- and far-field. Specific substrates have thus been designed for efficient low frequency Raman and reflectance contrast spectroscopies. By exploiting simultaneously optical interference and plasmonic resonance in these substrates, to enhance both elastic (reflectivity) and inelastic (Raman) scattering, accurate characterizations of the assemblies of silver nanocrystal have been performed. Determination of pertinent parameters at the nanoscale by these rapid nondestructive techniques was possible for appropriately designed architectures. In particular the potential for evaluating the size of the Ag nanoparticles by Raman analysis or from a simple reflectivity measurement was made possible by localizing the plasmon-resonant Ag NPs at maxima of the interference standing wave pattern. Moreover buried plasmonic architectures with subwavelength lateral sizes were fabricated, and their imaging with a resolution down to the limit of confocal optical microscopy was demonstrated.

Finally, the possibility to use these "3S−3D" substrates for SERS sensing has been demonstrated. They offer the advantage of exploiting in the visible range the strongest enhancement of silver nanoparticles, because they are buried in a matrix that avoids the dissemination of these highly toxic particles and simultaneously limits their alteration, while preserving their plasmonic properties. Another important advantage of these novel kinds of plasmon-active substrates is that they maintain flat and chemically inert surfaces. It is also interesting to note that standard wafers coming from Si-based technologies can be used. Here, the focus was put on the fabrication of optical sensing devices; however, most of the technical and physical ingredients could be easily employed for the fabrication of various plasmonic devices for nonlinear, photovoltaic, or wave-guiding applications.

METHODS

Embedded Ag Nanoparticle Patterns. Silver ions (Ag^+) of low energy (3−20 keV) have been implanted in a silica layer with fluencies ranging between 10^{15} and a few 10^{16} ions/cm^2. This was achieved by means of a specially modified Varian 200A2 implanter. The embedding dielectric is a silica layer thermally grown on silicon. Its thickness (240 nm) was chosen to obtain an amplification of the Raman efficiency under an oblique incidence. Different stencils containing different sized and shaped apertures (squares, slits, dashed slits) were prepared by focused ion beam milling of a 200 nm thick Si_3N_4 membrane, and then placed in contact with the SiO_2 surface.

Transmission Electron Microscopy. Cross-sectional (XS) and plan-view (PV) specimens were prepared for transmission electron microscopy (TEM) examination, by the standard procedure involving grinding, dimpling, and Ar^+ ion beam thinning until electron transparency. An FEI Tecnai microscope equipped with a field emission gun and a spherical aberration corrector and operating at 200 keV was used for imaging.

Optical Analyses. Reflectivity measurements were performed in quasi-normal incidence by using a Varian Cary 5000 spectrophotometer. The Raman signals have been collected in the far-field regime using a standard confocal microscope and a Jobin-Yvon Horiba T64000 spectrometer. The spectra were recorded with an unusual very large frequency range down to few centimeter^{-1} and using specific experimental conditions. The incident beam was focused under an oblique incidence, whereas the scattered beam was collected under the normal incidence. The 413 nm line (3.00 eV) of a Krypton laser was used as excitation light because it coincides with the plasmon resonance of the Ag NPs. During the scans, the laser power was fixed at 1 mW on the sample, the integration time was 0.2 s and the step 0.2 μm. Dark-field optical images have been recorded using a Jobin-Yvon Horiba Xplora spectrometer.

REFERENCES AND NOTES

1. Stewart, M. E.; Anderton, C. R.; Thompson, L. B.; Maria, J.; Gray, S. K.; Rogers, J.; Nuzzo, R. G. Nanostructured Plasmonic Sensors. *Chem. Rev.* **2008**, *108*, 494–521.
2. Anker, J. N.; Hall, W. P.; Lyandres, O.; Shah, N. C.; Zhao, J.; Van Duyne, R. P. Biosensing with Plasmonic Nanosensors. *Nat. Mater.* **2008**, *7*, 442–453.
3. Fleischmann, M.; Hendra, P. J.; McQuillan, A. J. Raman Spectra of Pyridine Adsorbed at a Silver Electrode. *Chem. Phys. Lett.* **1974**, *26*, 163–166.

4. Nie, S.; Emory, S. R. Probing Single Molecules and Single Nanoparticles by Surface-Enhanced Raman Scattering. *Science* **1997**, *275*, 1102–1106.
5. Le Ru, E. C.; Meyer, M.; Etchegoin, P. G. Proof of Single-Molecule Sensitivity in Surface Enhanced Raman Scattering (SERS) by Means of a Two-Analyte Technique. *J. Phys. Chem. B* **2006**, *110*, 1944–1948.
6. Atwater, H. A.; Polman, A. Plasmonics for Improved Photovoltaic Devices. *Nat. Mater.* **2010**, *9*, 205–213.
7. Zhao, Y.; Zhang, X. J.; Ye, J.; Chen, L. M.; Lau, S. P.; Zhang, W. J.; Lee, S. T. Metallo-Dielectric Photonic Crystals for Surface-Enhanced Raman Scattering. *ACS Nano* **2011**, *4*, 3027–3033.
8. Baker, G. A.; Moore, D. S. Progress in Plasmonic Engineering of Surface-Enhanced Raman-Scattering Substrates Toward Ultra-Trace Analysis. *Anal. Bioanal. Chem.* **2005**, *382*, 1751–1770.
9. Lacy, W. B.; Williams, J. M.; Wenzler, L. A.; Beebe, T. P.; Harris, J. M. Characterization of SiO_2-Overcoated Silver-Island Films as Substrates for Surface Enhanced Raman Scattering. *Anal. Chem.* **1996**, *68*, 1003–1011.
10. Beresna, M.; Kazansky, P. G.; Deparis, O.; Carvalho, I. C. S.; Takahashi, S.; Zayats, A. V. Poling-Assisted Fabrication of Plasmonic Nanocomposite Devices in Glass. *Adv. Mater.* **2010**, *22*, 4368–4372.
11. Moskovits, M. Surface-Enhanced Spectroscopy. *Rev. Mod. Phys.* **1985**, *57*, 783–826.
12. Zayats, A. V.; Smolyaninov, I. I. Near-Field Photonics: Surface Plasmon Polaritons and Localized Surface Plasmons. *J. Opt. A: Pure Appl. Opt.* **2003**, *5*, S16–S50.
13. Bacsa, W. S.; Lannin, J. S. Bilayer Interference Enhanced Raman Spectroscopy. *Appl. Phys. Lett.* **1992**, *61*, 19–21.
14. Kreibig, U.; Vollmer, M. *Optical Properties of Metal Clusters*; Springer-Verlag: Berlin, Heidelberg, 1995.
15. Evanoff, D. D; Chumanov, G. Synthesis and Optical Properties of Silver Nanoparticles and Arrays. *Chem. Phys. Chem.* **2005**, *6*, 1221–1231.
16. Rycenga, M.; Cobley, C. M.; Zeng, J.; Li, W.; Moran, C. H.; Zhang, Q.; Qin, D.; Xia, Y. Controlling the Synthesis and Assembly of Silver Nanostructures for Plasmonic Applications. *Chem. Rev.* **2011**, *111*, 3669–3712.
17. Jones, M. R.; Osberg, K. D.; Macfarlane, R. J.; Langille, M. R.; Mirkin, C. A. Templated Techniques for the Synthesis and Assembly of Plasmonic Nanostructures. *Chem. Rev.* **2011**, *111*, 3736–3827.
18. Carles, R.; Farcau, C.; Campos, J; Bonafos, C.; Benassayag, G.; Zwick, A. Low-Energy IonBeam Synthesis as a New Route toward Plasmonic Panostructures. *Materials for Nanophotonics—Plasmonics, Metamaterials, and Light Localization;* Brongersma, M. L., Dal Negro, L., Fukumoto, J. M., Novotny, L., Eds.; MRS Symposium Proceedings Series, Vol. 1182; Cambridge University Press: U.K., **2009**; pp EE09−21.
19. Carles, R.; Farcau, C.; Bonafos, C.; Benassayag, G.; Pecassou, B.; Zwick, A. Synthesis of Single Layers of Ag Nanocrystals by Ultra-low Energy Ion Implantation for Large Scale Plasmonic Structures. *Nanotechnology* **2009**, *20*, 355305.
20. P. Benzo, P.; Cattaneo, L.; Farcau, C.; Andreozzi, A.; Perego, M.; Benassayag, G.; Pecassou, B.; Carles, R.; Bonafos, C. Stability of Ag Nanocrystals Synthesized by Ultra-low Energy Ion Implantation in SiO_2 Matrices. *J. Appl. Phys.* **2011**, *109*, 103524.
21. Baida, H.; Billaud, P.; Marhaba, S.; Christofilos, D.; Cottancin, E.; Crut, A.; Lerm, J.; Maioli, P.; Pellarin, M.; Broyer, M.; et al. Quantitative Determination of the Size Dependence of Surface Plasmon Resonance Damping in Single Ag@SiO_2 Nanoparticles. *Nano Lett.* **2009**, *9*, 3463–3469.
22. Voisin, C.; Christofilos, D.; Loukakos, P. A.; Del Fatti, N.; Vallée, F.; Lermé, J.; Gaudry, M.; Cottancin, E.; Pellarin, M.; Broyer, M. Ultrafast Electron−Electron Scattering and Energy Exchanges in Noble−Metal Nanoparticles. *Phys. Rev. B* **2004**, *69*, 195416.
23. Drachev, V. P.; Chettiar, U. K.; Kildishev, A. V.; Yuan, H. K.; Cai, W.; Shalaev, M. V. The Ag Dielectric Function in Plasmonic Metamaterials. *Opt. Express* **2008**, *16*, 1186–1195.
24. Lou, N.; Groenen, J; Benassayag, G.; Zwick, A. Acoustics at Nanoscale: Raman-Brillouin Scattering from Thin Silicon-on-Insulator Layers. *Appl. Phys. Lett.* **2010**, *97*, 141908.
25. Johnson, P. B.; Christy, R. W. Optical Constants of the Noble Metals. *Phys. Rev. B* **1972**, *6*, 4370–4379.
26. Lynch, D. W.; Hunter, W. R. *Handbook of Optical Constants of Solids*; Palik, E. D., Ed.; Academic Press: New York, 1985; pp 350−357.
27. Palpant, B.; Portales, H.; Saviot, L.; Lerme, J.; Prevel, B.; Pellarin, M.; Duval, E.; Perez, A.; Broyer, M. Quadrupolar Vibrational Mode of Silver Clusters from Plasmon-Assisted Raman Scattering. *Phys. Rev. B* **1999**, *60*, 17107–17111.
28. Otto, A.; Timper, J.; Billmann, T.; Kovacs, G.; Pockrand, I. Surface Roughness Induced Electronic Raman Scattering. *Surf. Sci.* **1980**, *92*, L55–L57.
29. Bachelier, G.; Mlayah, A. Surface Plasmon Mediated Raman Scattering in Metal Nanoparticles. *Phys. Rev. B* **2004**, *69*, 205408.
30. Tsang, J. C.; Kirtley, J. C.; Theis, T. N. Long and Short Range Effects in Surface Enhanced Raman Scattering. *J. Chem. Phys.* **1982**, *77*, 641–645.